Investigation of breaking and non-breaking solitary waves and measurements of swash zone dynamics on a 5° beach

Lisa Smith[a], Atle Jensen[a], Geir Pedersen[a]

[a] *Department of Mathematics, University of Oslo, Norway*

Abstract

This study presents an experimental investigation of plunging breakers on a sloping beach with an inclination of 5.1°. The incident waves are solitary waves with various amplitudes from non-breaking waves to plunging breakers, and the area investigated is the swash zone. PIV (Particle Image Velocimetry) is performed on images captured at four different field of views (FOV). Shoreline position and maximum runup are measured, and are repeatable in both time and height, although cross-sectional variations of the shoreline shape are observed at maximum runup. For non-breaking waves the runup and fluid flow is computed by a boundary integral techniques combined with boundary layer model. Then, there is excellent agreement between the experimental and the computed velocity profiles at the lower region of the beach, while the boundary integral technique overpredicts the maximum runup height severely. For breaking waves the experiments indicate that the motion becomes more irregular as we move further up the beach. In addition, there are more irregularities present for waves with larger amplitude. Length and velocity of air bubbles entrapped by the plunging breakers are extracted from an image series captured with a large FOV. The images showed that a large air bubble remains intact for a time period during runup for the breaking waves.

Keywords: Breaking solitary waves, PIV, Boundary layers, Runup, Bubble entrainment.

1. Introduction

In shallow water with constant depth, the nonlinear effect and dispersion will be balanced for solitary waves (Peregrine, 1983). During shoaling the wave will steepen, and at some critical point breaking may occur. Wave breaking is one of the most important physical features in the swash zone (Elfrink and Baldock, 2002). Breaking waves have a large impact on sediment transport onshore, which can result in beach erosion and affect construction located near the shore. Although breaking waves is a well-known phenomenon from our daily life, many physical aspects regarding wave breaking are still poorly understood.

Several experimental studies of breaking waves have been performed in the recent years. A broad range of different experimental methods have been utilized to measure quantities such as surface elevation, runup, shear stress, and velocities. Techniques such as Laser Doppler Velocimetry (Petti and Longo, 2001), PIV (Cowen et al., 2003) and application of shear sensors (Barnes et al., 2009) have been utilized. The swash zone is the region where the beach is partly wetted during runup and draw-down. Aeration and the small flow depth makes the swash zone a challenging region to study experimentally with the techniques mentioned above. A further development of the PIV method is Bubble image Velocimetry (BIV), which Rivillas-Ospina et al. (2012) use to investigate velocity fields in plunging breakers. They compared the measurements with numerical simulations conducted with Reynolds Average Navier Stokes Equations Model. The model gave fairly good agreement with the measurements in the surf zone, but the model overpredicted the velocities in the swash zone as compared to the BIV measurements.

Surf zone dynamics for non-breaking solitary waves on a steep beach were investigated experimentally and theoretically by Pedersen et al. (2013). Boundary layer profiles were measured by PIV and good agreement with theory was obtained for regular flows. However, for larger amplitudes and far from the equilibrium shoreline undulations and rollers were observed. Velocity fields underneath shoaling solitary waves in the surf zone has recently been studied by Lin et al. (2014) and Lin et al. (2015). The first study shows PIV measurements from a wide area of the surf zone for waves with various normalized amplitude. The latter study presents detailed high resolution PIV boundary layer measurements of one shoaling solitary wave.

One of the latest work on solitary waves on a plane beach has been conducted by Pujara et al. (2015). They investigated the flow evolution of the runup and draw-down of solitary waves in the range from non breaking to plunging breakers. A shear plate was located at different positions along the beach and measurements revealed that the maximum positive bed shear stress was obtained in the tip of the swash tongue during runup, and was due to the evolution of a boundary layer and bore driven turbulence. The maximum negative bed shear stress was obtained at the end of the withdrawal. The flow is accelerated during downrush by gravity and the bed shear stress increases during draw-down until a maximum was reached right before the water ran out of the measuring area.

Until now, PIV measurements with high temporal resolution close to the beach have not been reported for plunging breaking waves in the swash zone. The present article presents PIV measurements for solitary waves, of different amplitudes, that ranges from non-breaking to plunging cases on a beach with inclination $5°$. Some of the techniques are adopted from the study of non-breaking waves in Pedersen et al. (2013), but the present investigation is more demanding due to longer swash zones and the presence of irregular flow and air bubbles due to the breaking. The article starts with a description of the experimental set-up and the computational Boundary Integral Model used in this study (chapter 2). Further on, measured and computed results will be presented; the surface elevation of the incident waves in chapter 3.1, surface development and maximum runup in chapter 3.2, velocity profiles from the swash zone in chapter 3.3, and air bubble investigation in chapter 3.4. Finally, a discussion of the findings will be presented in chapter 4.

2. Experimental set-up and formulation

2.1. The wave tank

The experiments were conducted in a 25 m long and 0.51 m wide wave tank located at the Hydrodynamics Laboratory at the University of Oslo. Incident waves were generated in an equilibrium depth of $H = 20.5$ cm

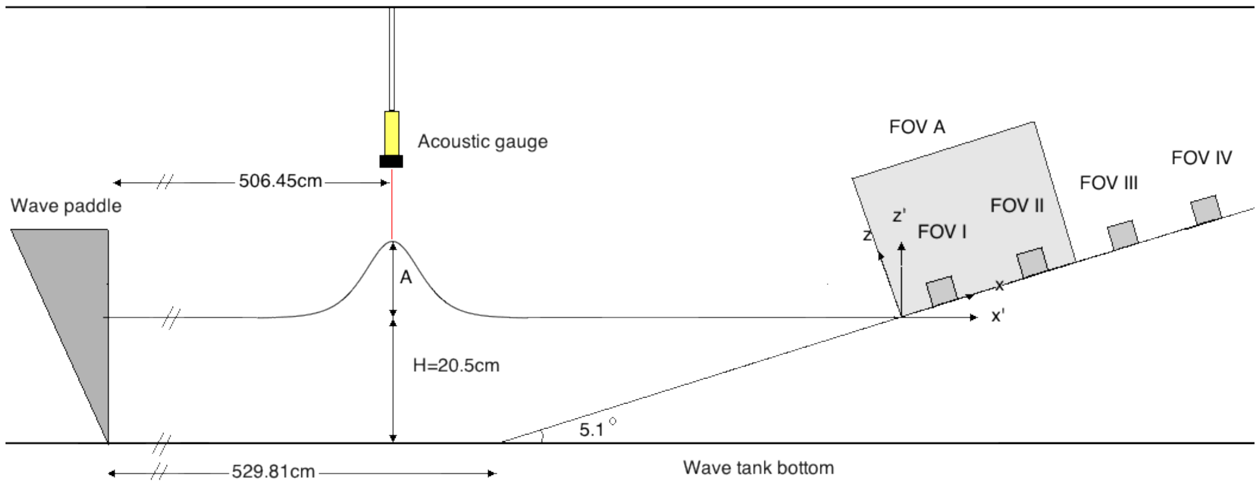

Figure 1: *Sketch of the experimental set-up.*

by a piston type wave maker using the method described in Jensen et al. (2003). A PETG (Polyethylene Terephthalate Glycol-modified) beach with an inclination of 5.1° was placed in the wave tank with its toe 529.81 cm from the start position of the wave paddle. Two coordinate systems are introduced, one parallel to the still water level (x', z'), and one parallel to the beach (x, z) (see Figure 1). The origin of both is at the equilibrium shoreline.

The amplitude to depth ratios should equal $(\alpha = 0.10, 0.12, 0.20, 0.30, 0.40, 0.50)$, however, imperfection in the generation and frictional effects along the wave tank reduced the heights slightly such that the amplitude in front of the beach, A, became slightly less than αH. An acoustic wave gauge (ultra Banner U-Gage S18U, sample frequency of $200Hz$) measured the wave height at the toe of the beach and the Boundary Integral Method (BIM) was used to correct for the influence of the reflected wave. The resulting amplitudes are given in Table 2.

2.2. Instrumentation, measurements

To obtain velocity fields in the swash zone, high speed video was recorded at four different field of views (FOV), located upward along the beach (Table 1). The water in the tank was seeded with polymid particles with diameters of approximately 50 μm. A Quantronix Darwin Duo pulsed laser generated a light sheet parallel to the centreline of the wave tank, and a Photron SA5 high speed camera (1024 x 1024) synchronized with the laser, captured images of the illuminated particles. A Carl Zeiss Makro- Planer 2/50 zf (50 mm) lens was used. Images were collected at 3000 frames per seconds (fps). The image processing were performed in DigiFlow (Dalziel, 2006). PIV was performed using interrogation windows of 32 x 8 pixels with a 75% overlap. Oblong interrogation windows are beneficial in boundary layer flow and have been employed previously in Liu et al. (2007) and Pedersen et al. (2013). A temporal averaging of 10 images was applied to reduce noise from the data. No differences in the measurements were obtained when velocities from an averaging of 10 and 15 images were compared to each other. This implies that a temporal averaging

FOV:	I	II	III	IV
Location, x:	[8.49 - 13.04]	[36.35 - 40.26]	[77.55 - 81.53]	[117.76 - 121.80]
Location, z:	[-0.05 - 3.78]	[-0.16 - 3.54]	[-0.04 - 3.79]	[-0.85 - 3.09]

Table 1: *Location of the different FOVs in cm. The dimensions of the FOVs are approximately 4 cm x 4 cm.*

of 1/305 s (10 images) is acceptable. The errors related to the PIV algorithm are described in detailed in Raffel et al. (2013). The average particle image diameter for a randomly chosen image from this experiment was found to be approximative 3.16 pixels. This is close to the optimal particle size that minimizes the PIV error related to peaklocking. The high capturing rate allows us to investigate large velocity without large pixel displacements preventing aliasing, and also the high temporal resolution minimize the error concerning out of plane motion. If there is no loss of particles, and the particle distribution is uniform, the PIV error can be limited to 0.05 pixels (Kähler et al., 2016). This corresponds to an error of approximately 0.5 cm/s for instantaneous measurements. The averaging in time applied to the measurements will reduce this error.

To investigate air bubbles encapsulated by the plunging breakers, the camera was moved further away from the wave tank, resulting in much larger FOV than the FOVs installed to obtain velocity fields. This FOV will be referred to as FOV A and covers $0\,\text{cm} < x < 60\,\text{cm}$. The frame rate was reduced to 500 fps and a continuous dedolight 400D was used as illumination, replacing the laser. A white background sheet was attached to the side wall of the wave tank and the water was dyed dark blue to increase the contrast of the images.

The maximum runup was measured by capturing images of the shoreline at its maximum position. A high speed Photron APX camera was mounted on rails above the beach in the wave tank with same inclination as the beach. A high pulsed white light was used as illumination. The camera captured 125 frames per second, and the maximum shoreline profiles were tracked manually for each wave.

All the experiments were repeated at least three times to assure repeatability (N=3). However, we emphasize that this is insufficient for determination of a standard deviation, let alone extraction of turbulent intensities. The scatter δ_i for some measured quantity x_i, is then calculated in the following manner,

$$\delta_i = \frac{x_i - \overline{x}}{\overline{x}}, \tag{1}$$

where $\overline{x}$ is the mean over the repetitions.

To find a measure of the irregularities present in the PIV measurements, the deviations of the velocities are calculated for the strongest plunging breaker. Deviations are extracted at times where the mean flow, u, in an area near the beach has a velocity close to either 40, 0 or -40, all measured in cm/s.

$$\sigma = \sqrt{\frac{1}{N-1}\sum_{i=1}^{N}(x_i - \overline{x})^2}, \tag{2}$$

where N is the number of repetitions. It is remarked that while σ is computed by the formula for standard deviation it may only be conceived as a rough estimate of repeatability and regularity due to the small value for N. The average deviations in the z-direction are calculated from the area ($0\,\text{cm} < z \leq 0.6\,\text{cm}$)

$$\overline{\sigma} = \sqrt{\frac{1}{M}\sum_{j=1}^{M}\sigma_j^2}, \tag{3}$$

where M corresponds to number of grid points in the given z-range.

2.3. The potential flow and boundary layer models

The evolution of the waves during shoaling, as well as the runup for the smallest amplitude, were computed by a BIM (Boundary Integral Model) for inviscid flow (Pedersen et al., 2013). This model may accurately describe the runup of fully nonlinear non-breaking waves and the evolution of plunging breakers. However, the model breaks down when a plunger re-attaches with fluid or impacts the beach. Moreover, the model becomes singular when the contact angle at the shoreline exeeds 90° and the results become unreliable for contact angles slightly smaller than this. As a consequence a maximum runup height from the BIM model is obtained only for $\alpha = 0.10$.

The potential flow model also provides the outer flow and the pressure gradient which are used as input to a FDM viscous boundary layer model. However, the coupling between the models is only one way as there is no feed-back from the boundary layer to the potential flow model. More details on both models are given in Pedersen et al. (2013).

For $\alpha = 0.1$ a refinement of the spatial grid resolution from a typical value of $0.14H$ to half this size gave a change of 0.9% in the runup height. Since the BIM model is of fourth (space) and third (time) order this point to an error for the finer resolution which is much smaller than 1%. The same resolutions were applied to the breaking waves. For all the waves the temporal increment for the finest grid was 0.0073 s, which is twice as large as the temporal averaging interval used in the PIV processing. The viscous boundary layer model generated 600 grid points along the beach, with a spatial increment of $0.0042H$. The time resolution was kept the same as for the BIM.

3. Results

Visual inspection of the experiments revealed that the cases with normalized amplitude $\alpha = 0.10$ and $\alpha = 0.12$ did not break until the draw-down, while all the other cases developed into plunging breakers at, or before, the equilibrium shoreline. The plunging breakers encapsulated large amounts of air, which resulted in air bubbles in the swash tongue of the breaking waves (Figure 2).

3.1. Surface elevation of the incident waves

The amplitude of the smallest wave is determined by a simple correction scheme. First the maximum of the series from the acoustic gauge A_m is used as solitary wave amplitude in the BIM model. For the lowest wave this value is $A_m/H = 0.0998$. When BIM data are extracted at the gauge position we obtain

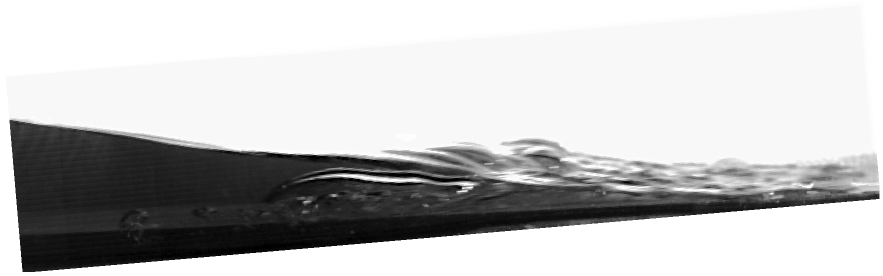

Figure 2: *Image of the swash tongue for $\alpha = 0.30$. The camera is tilted with the same inclination as the beach, and the swash tongue propagates from left to right.*

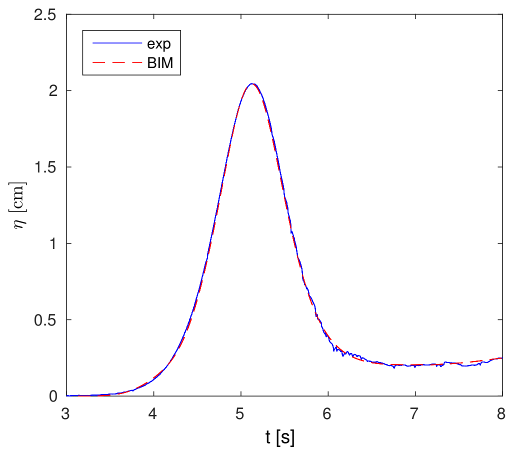

Figure 3: *Measured and computed surface elevation for $\alpha = 0.10$.*

a slightly too large surface elevation $A_b = 0.1008$, due to the reflection from the beach. We then adjust the amplitude according to $A = A_m(1 - \frac{(A_b - A_m)}{A_m})$. The result is $A/H = 0.09865$ and the comparison with BIM results, obtained with this amplitude for the incident wave, is shown in Figure 3. The surface elevation measurements are in close agreement with computed surface elevation from the BIM simulations. When the surface elevation of the incident waves are very steep, the ultra sonic signal will not get reflected back and registered by the sensor. This leads to dropouts in the measurements, which have been filled in by linear interpolation. Cubic polynomial regression is used to remove noise from the signal. The corrected and measured amplitudes for all the waves are given in Table 2.

3.2. Surface development and maximum runup

BIM simulations of the near-shore evolution model is shown in Figure 4. For reasons explained previously (section 2.3) we only compute the runup for the smallest wave, $\alpha = 0.10$. For the other cases shown the numerical model describes the evolution of the plunger, but nothing beyond its impact onshore.

For $\alpha = 0.10$ the computed time, inundation length and height for maximum runup were $t = 8.93\,\text{s}$, $r = 112.78\,\text{cm}$ (measured along the beach), and $R/A = 4.95$ respectively. Comparing this the the measurements in Table 2 we observe that the theoretical runup height is 30% too large and and occurs 0.07 s later. Pedersen

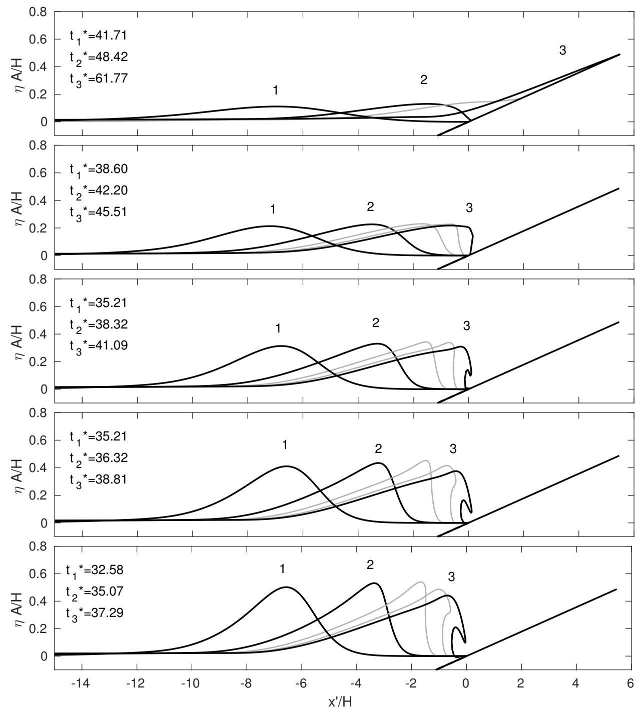

Figure 4: *BIM simulation of the waves the upper to lower figures correspond to* $\alpha = (0.10, 0.20, 0.30, 0.40, 0.50)$*, respectively. In the top panel the curve marked 3 corresponds to the time of maximum runup.*

et al. (2013) reported differences that were similar, but smaller, deviations between experiments and potential flow soloutions which they suggested were caused by the lack of viscous effects and surface tension in the model. The dicreapancies of Pedersen et al. (2013) were presumably smaller than those herein because the beach was steeper in the reference (10.54°) which led to thicker flow depths and shorter inundations. In fact, in Figure 5 we observe transverse variations in the field of views. The average runup height, over the FOV, for the smallest wave ($\alpha = 0.10$) is 84.07 cm. This is 3.76% smaller than the maximum one, but the total cross-beach average, which is not available, is presumably even smaller. This implies that real difference between theoretical and computed runup is larger than indicated by the maximum values. Table 2 shows that the maximum runup is fairly repeatable for all waves including the breaking ones.

The shoreline at maximum runup are shown in Figure 5. It is fairly repeatable for the amplitude close to 0.1 times the depth, but has a wedge-like shape. This is presumably due to a cross-wise deformation of the beach which has been measured using a straightedge and a feeling gauge. The typical maximum suppression in each transect of the beach was 3 mm. If we assume that the depressions were unsystematic and that the later stages of runup are governed by gravity alone (see, for instance, Jensen et al. (2003)) this should correspond to a variation of 3 cm on a 1 in 10 slope beach. However, even though the flow depth is small during runup, the momentum transport due to the pressure is still noticeable (inferred from the simulations, results not shown). More importantly, there is a systematic suppression at the center-line of the beach and the beach width is 51 cm, which is comparable to the inundation length for the smallest amplitude. Hence,

α	A/H	A_m/H	r/H	R/A	$e_r[\%]$	$t[s]$	$e_t[\%]$
0.10	0.0986	0.0998	4.26	3.82	1.68	8.86	0.15
0.12	0.1184	0.1194	5.15	3.85	0.27	8.67	0.15
0.20	0.1977	0.1984	7.19	3.22	0.93	8.53	0.31
0.30	0.2959	0.2967	9.35	2.80	1.08	8.03	0.78
0.40	0.3930	0.3936	11.09	2.50	0.11	7.82	0
0.50	0.4863	0.4869	13.05	2.37	2.27	7.30	1.64

Table 2: *Amplitudes and runup. A is the incident wave amplitude, A_m is the maximum measured surface elevation at the toe of the beach, r is the inundation length , R is the vertical maximum runup, t is the time corresponding to max runup and e is the estimated deviation in the measurement.*

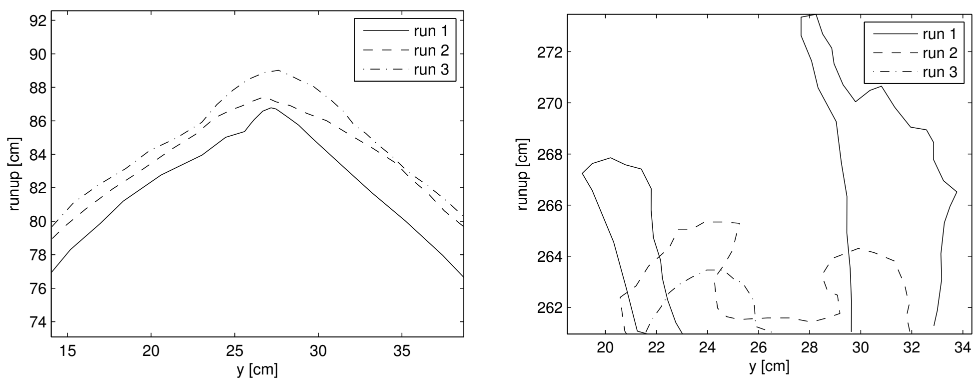

Figure 5: *Cross-sectional variation of the shoreline shapes at max runup. Left:* $\alpha = 0.10$*, Right:* $\alpha = 0.50$.

another relevant estimate of the runup variation is the suppression times the contact angle (angle of fluid wedge during runup) in *radians*. In the simulations this angle approaches 0.5° at maximum runup, which yields a variation in x of 30 cm. This is modified by surface tension that affects the contact angle and shape of fluid body near the shoreline. Unfortunately, we cannot quantify this effect from the experiments. From Figure 5 it is clear that transverse variation is larger than the first estimate, but smaller than the latter one. The runup varies much more for the three repetitions of the breaking wave $\alpha = 0.50$, resulting in irregularly shaped shorelines (Figure 5).

An estimate of the arrival time of the wave for FOV II, III and IV, were calculated from intensity changes in the image captured at the different FOV. Each image in each time series was compared to the initial image taken before the wave paddle starts. The image where the sum of the light intensity differs more than a given threshold from the initial image, correspond to the time when the wave enters that FOV. The measured shoreline positions as a function time are presented in Figure 6. The maximum error obtained for three different runs was 0.18%. This indicate that the shoreline motion was repeatable for each of the FOV.

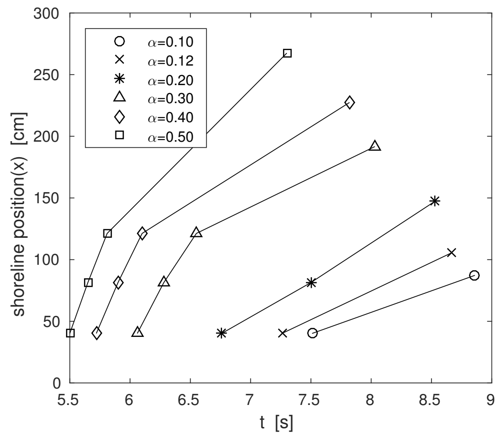

Figure 6: *Shoreline position as a function of time for all wave height. The first measurements correspond to the swash tongue arrival time for FOV II, III, IV. The last measuring point for all cases correspond to measurement of maximum runup.*

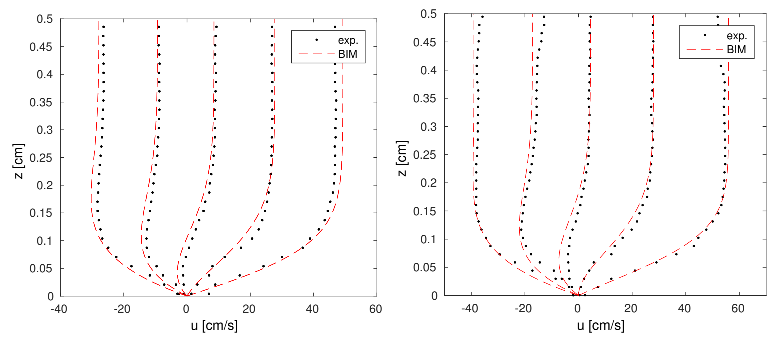

Figure 7: *Velocity profiles for* $\alpha = 0.10$.
Left: FOV I $x = 8.7$ *cm* $t = [7.48, 7.82, 8.15, 8.48, 8.81]$ *s.*
Right: FOV II $x = 40.1$ *cm* $t = [7.76, 8.10, 8.76, 9.10]$ *s.*

3.3. Velocity profiles from the swash zone

Velocity profiles are extracted from the PIV data that are obtained from the four different FOVs, approximately from 10 cm to 120 cm from the equilibrium shoreline. In Figure 7 we observe that computed (BIM) and measured (PIV) velocity profiles agree for $\alpha = 0.10$ in FOV I and II. The maximum deviation between measured and computed outer flow occured at the beginning of PIV timeseries and was 4.7% and 6.8% for FOV I and II (not shown), respectively. The deviations decreased for both FOVs as time increased. This complies with corresponding results in Pedersen et al. (2013) where the delay of the experimental wave was linked to capillary effects, while an accumulative reduction of velocity, and hence runup height, was related to the viscous boundary layers further up the beach. Hence, the BIM computation over-predicts the maximum runup as given in the previous section. The velocity deviation between the experimental runs for $\alpha = 0.10$ was average over the entire FOV and deviation was found to be $0.16\,\mathrm{cm}/s$. This is an indication of the overall experimental and PIV error related to this study.

The PIV analysis of the breaking waves was difficult due to air bubbles in the flow, and due to challenges

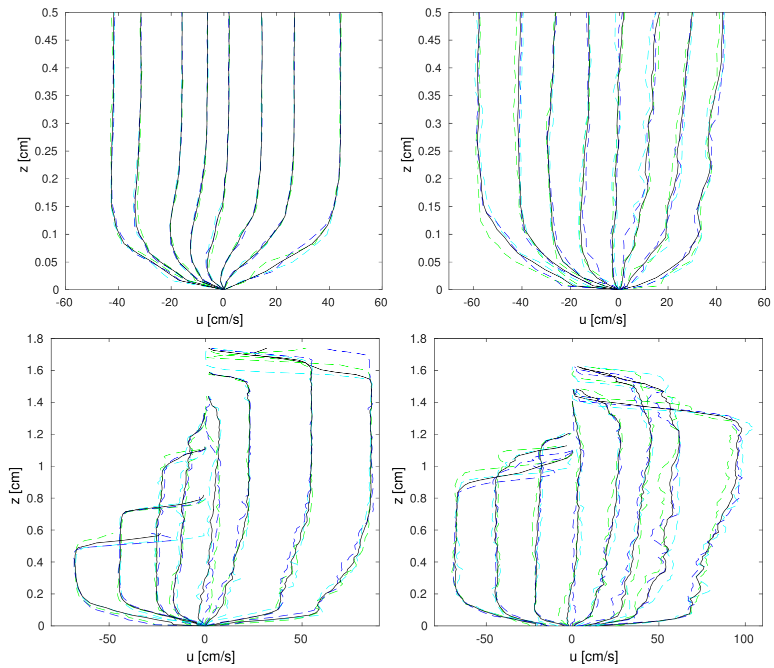

Figure 8: *Velocity profiles for* $\alpha = 0.50$. *Colors: blue, cyan and green correspond to run 1,2 and 3.*

Upper Left: FOV I $x = 8.7cm$ $t = [6.12, 6.34, 6.50, 6.69, 6.84, 7.00, 7.27, 7.45]$ *s.*

Upper Right: FOV II $x = 40.1cm$ $t = [6.43, 6.57, 6.74, 6.92, 7.14, 7.36, 7.56, 7.80]$ *s.*

Lower Left: FOV III $x = 81.4cm$ $t = [6.34, 6.60, 6.94, 7.12, 7.34, 7.50, 7.80, 8.16]$ *s.*

Lower Right: FOV IV $x = 121.2cm$ $t = [6.50, 6.78, 6.94, 7.10, 7.32, 7.60, 7.91, 8.20]$ *s.*

FOV	$u \sim 40\,\frac{\text{cm}}{\text{s}}$	$u \sim 0\,\frac{\text{cm}}{\text{s}}$	$u \sim -40\,\frac{\text{cm}}{\text{s}}$
I	1.04	0.33	0.67
II	1.13	0.65	1.12
III	2.26	1.11	1.06
IV	3.88	2.00	0.97

Table 3: *The irregularity measure, $\overline{\sigma}$, for $\alpha = 0.50$.*

with particle seeding within the thin swash zone. The case $\alpha = 0.50$ has the longest runup of all the breaking waves, and that makes it the one for which most data can be extracted from all the FOVs. Velocity profiles for $\alpha = 0.50$ are shown in Figure 8. The velocity profiles are extracted at times after all the air bubbles have passed each of the FOV. It is clear that the velocities at FOV I resembles the velocities obtained for $\alpha = 0.10$. The boundary layer is well defined and the deviation between the different runs is really small. For FOV II-IV the deviations tend to increase. However the largest irregularities are in the runup phase, while they decreases in the retreating flow. Hence, the withdrawal phase has a more regular boundary layer and a well defined outer flow for all the FOVs. The scatter parameter $\overline{\sigma}$, defined in Equation (3) is presented in Table 3. The deviations in the table for $\alpha = 0.50$ are larger in the locations far up the beach, in agreement with Figure 8. This may indicate that the flow in the upper surf zone is more irregular.

The velocities near flow reversal for all the different wave amplitudes will be discussed in the following. FOV II is located approximately 40 cm from the origin, and velocity profiles obtained from this FOV are shown in Figure 9. For $\alpha = 0.20$ the particle density was too sparse close to the surface, which led to spurious vacillations in the velocity profiles near $z \approx 1$. Some distance below the surface a region of uniform flow is apparent for all cases. Boundary layers are apparent for all the cases and they all display a flow reversal prior to that of the outer flow. However, the evolution of the boundary layers for $\alpha \leq 0.2$ and those for $\alpha \geq 0.3$ differ. The boundary layers for the higher amplitudes appear more irregular with a thicker and less pronounced region of reversed flow in the boundary layers. While the boundary layer for the lower amplitudes, including that of $\alpha = 0.20$, appears laminar the higher waves have boundary layers that presumably are in a transition to turbulence.

FOV III is located about 80 cm from origin along the beach. For $\alpha = 0.10$ and $\alpha = 0.12$, the swash tongues were too thin, and particles within the tongue were impossible to detect. Consequently, only $\alpha = 0.20 - 0.50$ will be presented for this FOV. None of the cases had an outer flow with constant velocity at times close to outer flow reversal (see Figure 10). This indicates that the motion was more irregular for this FOV than for FOV II.

FOV IV is located about 120 cm from where the still water reaches the beach. At this FOV, only $\alpha = 0.30 - 0.50$ will be presented due to the thin swash tongue for the other waves. Velocity profiles are given in Figure 11. The velocity was less repeatable at this location than for the other FOVs. The velocity profiles were more irregular, especially for $\alpha = 0.50$, where the average velocity profile obtained before

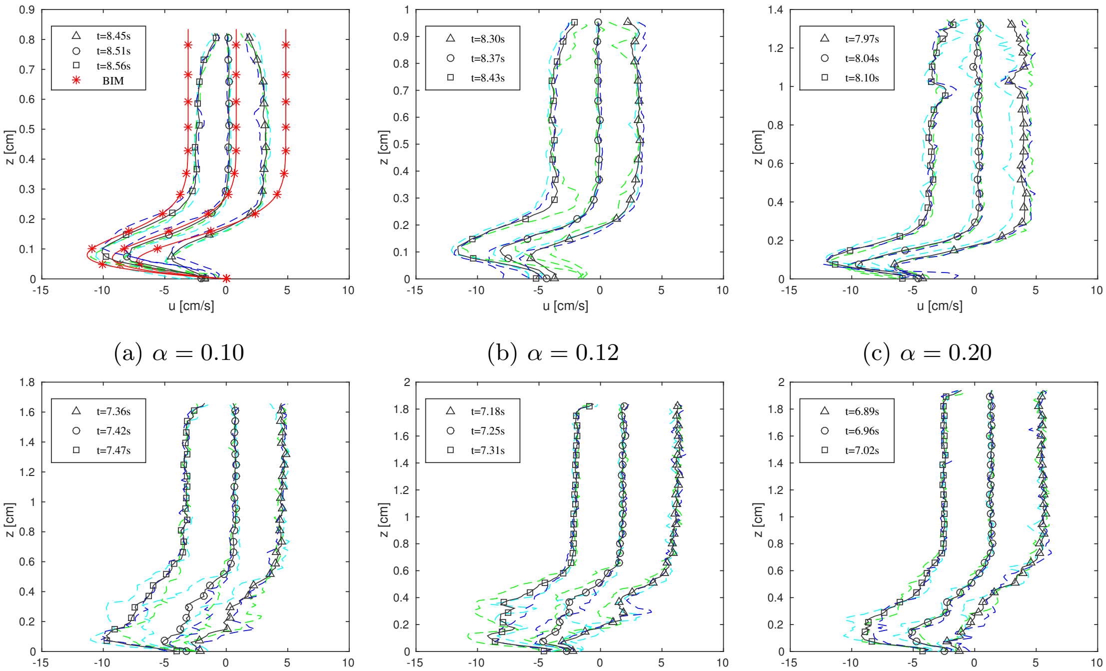

(a) $\alpha = 0.10$ (b) $\alpha = 0.12$ (c) $\alpha = 0.20$

(d) $\alpha = 0.30$ (e) $\alpha = 0.40$ (f) $\alpha = 0.50$

Figure 9: *FOV II, mean velocity profiles before and after the outer flow reverses (△,◯,□). Colors: blue, cyan, green and red correspond to run 1,2,3 and BIM respectively.* $x = 40.1$ *cm.*

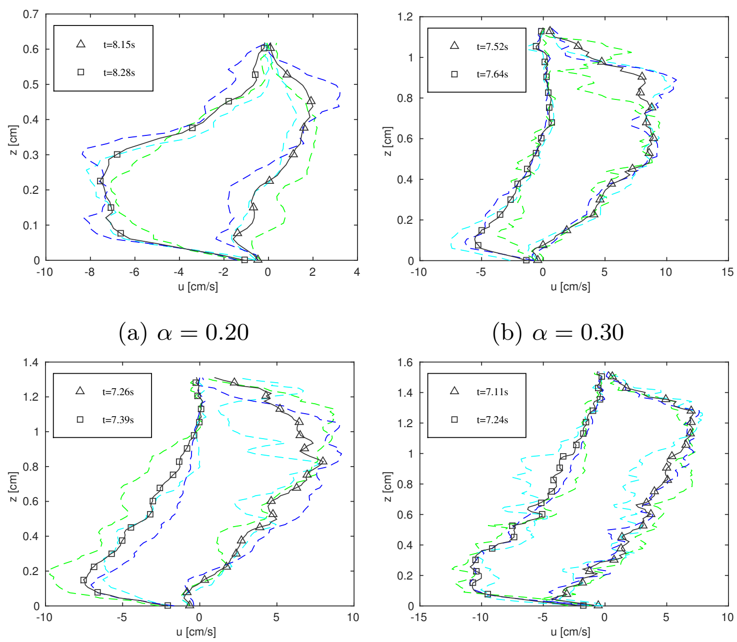

(a) $\alpha = 0.20$ (b) $\alpha = 0.30$

(c) $\alpha = 0.40$ (d) $\alpha = 0.50$

Figure 10: *FOV III, mean velocity profiles before and after the outer flow reverses (△,□). Colors: blue, cyan and green correspond to run 1,2 and 3.* $x = 81.4$ *cm.*

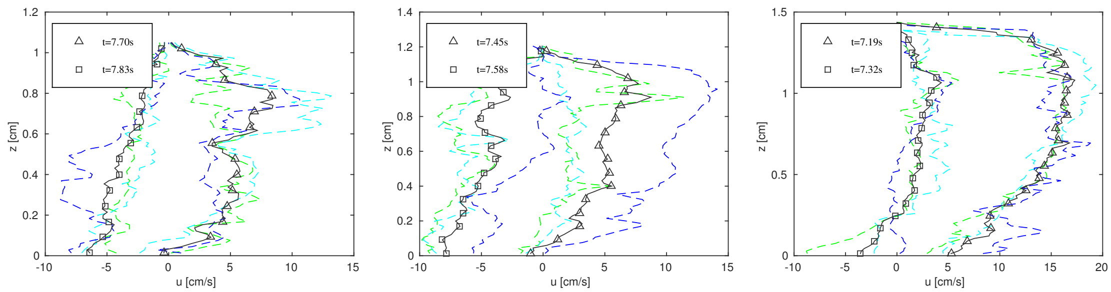

(a) $\alpha = 0.30$ (b) $\alpha = 0.40$ (c) $\alpha = 0.50$

Figure 11: *FOV IV, mean velocity profiles before and after the outer flow reverses (△,□). Colors: blue, cyan and green correspond to run 1,2 and 3.* $x = 121.2$ *cm.*

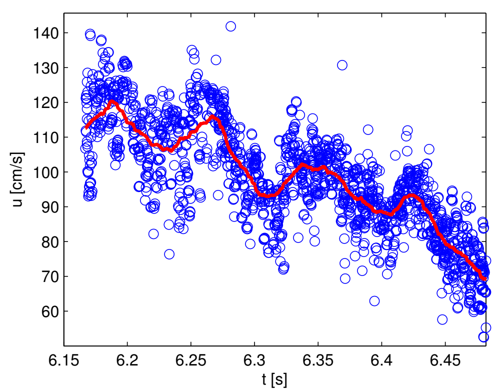

Figure 12: *FOV IV Collection of velocities of particles within a distance of* 0.05 *cm from the point* $(x, z) = (120, 0.3)$ *cm. The data is collected from* $\alpha = 0.50$*, run 2. Blue circles: Raw data points. Red line: 2 order interpolation with 40 evaluation points.*

flow reversal is reminiscent of the parbolic velocity profiles from fully developed turbulent channel flow, as described in White and Corfield (2006). Since the irregularity increases with distance from the equilibrium shoreline it is likely inherited from the breaking processes. Pedersen et al. (2013) claimed possible instabilities in the upper part of the swash zone for runup of non-breaking waves on a $10.54°$ beach. Moreover, in a study of boundary instabilities in the boundary layer under solitary waves Verschaeve and Pedersen (2014) concluded that instabilities were generally present in retarded boundary layer flows under waves. The crucial point is then if the noise level and growth potential, together, make the flow perturbations significant. Due to the gentler slope and the noise due to breaking one would anticipate that the waves on the present beach are prone to instability than those on a $10°$ beach. Instability, leading to flow transition is definitely a possible explanation for the increased irregularity. However, in Figure 11 the boundary layer thickness is comparable to the total flow depth which may be an important difference from the cases described in the references.

Inspection of videos of the front of the swash tongue from FOV IV (furthest up the beach) indicates that a systematic swirling effect were present in the front of the swash tongue for $\alpha = 0.50$. To investigate this phenomenon, Particle Tracking Velocimetry (PTV) has been utilized on images captured close to arrival of the swash tongue (5.33 s). There were sparse particle seeding in the front of the tongue, and the first time where enough particles were present for an ensemble PTV analysis, was at $t = 6.16\,\mathrm{s}$. This is still long before the large bubble arrives at this FOV. For each image pair after this, the velocity for all the particles within a distance of $0.05\,\mathrm{cm}$ from a given evaluation point $(x, y) = (120\,\mathrm{cm}, 0.3\,\mathrm{cm})$ are assessed. Figure 12 shows how the velocities vary as a function of time. Superimposed a steady deceleration of the fluid there is an oscillation. Flow in decelerating boundary layers are prone to instabilities, as mention above. However, the oscillations do not increase in magnitude and are present from the beginning and do thus not appear to be the result of any instability. Hence, it is plausible that the wave breaking induces irregularities, possibly in the form of vortices, that prevails during the subsequent motion.

3.4. Bubble investigation

For the plunging breakers ($\alpha = 0.20 - 0.50$) one large air bubble is encapsulated. As the waves propagated upward the beach, this bubble disintegrated into smaller and smaller bubbles. Before maximum runup, all the bubbles have escaped the surface. The images captured with the large FOV A provides some information about this air bubble formation (see Figure 13 and 14). To enhance the shape of the bubbles the gradient magnitude image is represented. This image technique will enhance sharp interphases between air and water, and accentuate the contour of the air bubbles. The shape of the main bubble is oval with a thin tongue in the front, for $\alpha = 0.30$. The inconsistency in front of the swash tongue, is a 3D effect due to a slightly tilted camera, and may be interpreted as the roughness of the surface. The shape of the main air bubble appears to be less repeatable for $\alpha = 0.50$. In particular, in run 2 the large air bubble cannot be identified in the image at all. The length of the main bubble for three different runs is given in Table 4. It is clear from the images and Table 4, that the three different runs are more similar for $\alpha = 0.30$ than for $\alpha = 0.50$. This supports the assertion that larger plungers are more irregular.

The air bubble velocity in the direction along the beach is given in Table 5. The largest velocities were obtained in the front of the bubbles for most of the runs, and may explain the shape of the thin tongue in the front of the air bubble observed for $\alpha = 0.30$. The bubbles velocities can be compared to the velocities of the developing shoreline (Figure 6). The average shoreline velocity from FOV II to FOV III was found to be $1.87\,\mathrm{m/s}$ for $\alpha = 30$ and $2.75\,\mathrm{m/s}$ for $\alpha = 50$, and the average is taken within a time interval close to the times of the bubble investigation. The average shoreline motion was smaller than the average bubble velocity for $\alpha = 30$, which interpret that the bubbles will not be lagged relative to the swash tongue for this wave, and the bubbles may not affect the later stages of the runup as much as first assumed. However for $\alpha = 0.50$ the average bubble velocity is smaller than the shoreline velocity which extends the area where air bubbles are present.

4. Discussion

For runup of non-breaking solitary waves on a 5.1° slope we observe laminar boundary layers. The presumption of laminarity is supported by the good agreement found with boundary layers computed by

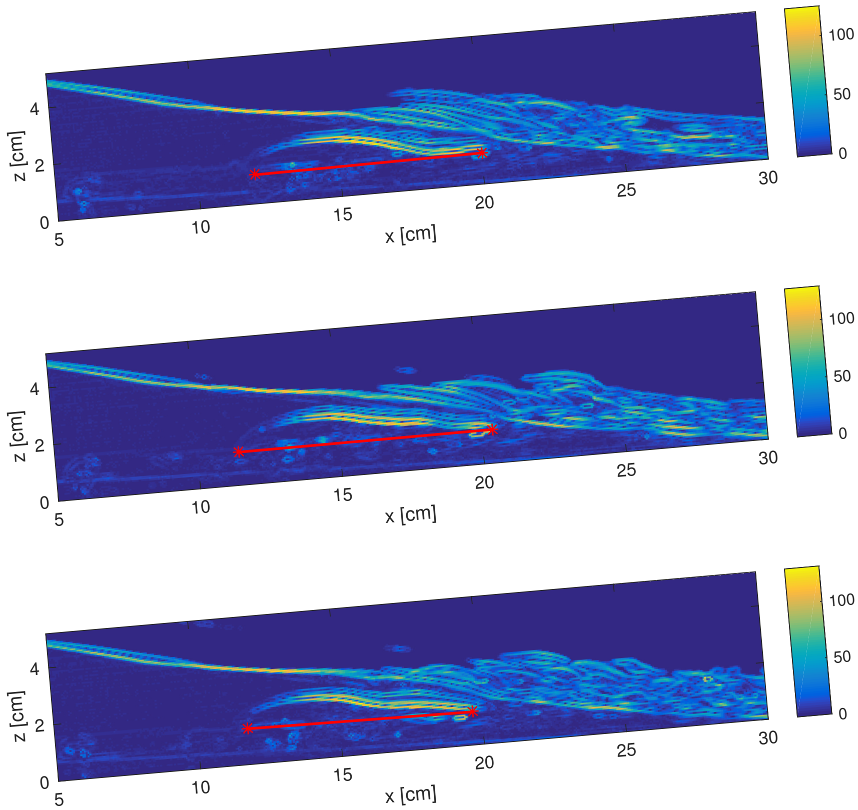

Figure 13: *Gradient magnitude images of the swash tongue for* $\alpha = 0.30$*, run 1, 2 and 3.* $t = 6.06\,s$*. The red line shows the length of the main air bubble.*

Main bubble size	**Run 1 [cm]**	**Run 2 [cm]**	**Run 3 [cm]**
$\alpha = 0.30$:	8.00	8.94	7.90
$\alpha = 0.50$:	9.24		8.17

Table 4: *Size of the main bubble measured at* $t = 6.06\,s$ *for* $\alpha = 0.30$*, and* $t = 5.54\,s$ *for* $\alpha = 0.50$.

$\alpha = 0.30$	Run 1	Run 2	Run 3
Front velocity [m/s]	2.05	2.20	2.48
Tail velocity [m/s]	2.10	2.05	2.23
$\alpha = 0.50$			
Front velocity [m/s]	3.26		2.01
Tail velocity [m/s]	1.58		2.23

Table 5: *Velocities along the beach for the main air bubble.* $t = 6.06\,s$ *for* $\alpha = 0.30$*, and* $t = 5.54\,s$ *for* $\alpha = 0.50$.

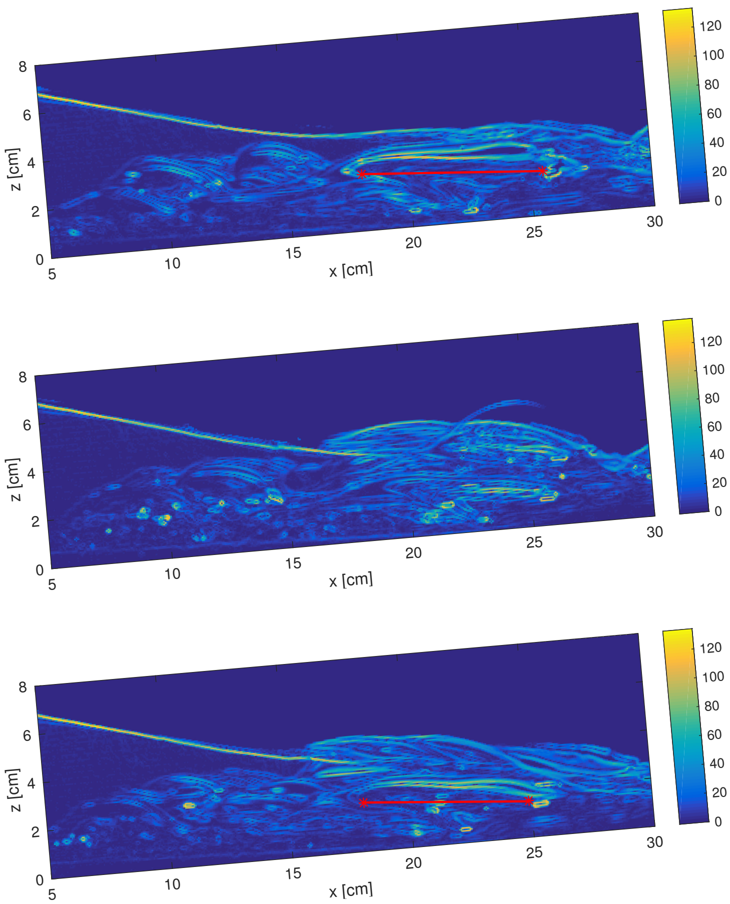

Figure 14: *Gradient magnitude images of the swash tongue for* $\alpha = 0.50$*, run 1, 2 and 3.* $t = 5.54\,s$*. The red line shows the length of the main air bubble.*

combining a potential flow model with a standard boundary layer model on the beach. However, in accordance with Pedersen et al. (2013) the potential flow model overpredicts the maximum runup height by 30%. The discrepancies between computations and measurements, which probably are due to viscosity and capillary effects, are in reality larger since tiny deformation of the beach increases the maximum runup height in the experiments.

The measurement of the breaking waves showed that the fluid motion becomes more irregular and less repeatable as we move further up the beach. In addition, the motion was more irregular for the waves with the stronger plunger than for those with smaller amplitude. The maximum runup was fairly repeatable, but marked an irregular transverse variations were observed for the breaking waves. The bubble investigation indicated that the air bubble shapes were repeatable for the waves with amplitude $\alpha = 0.30$ but not for the waves with amplitude $\alpha = 0.50$. Overall, irregular motion increases with larger breaking waves and as the waves propagate upwards the beach.

The present experiments are performed on relatively small scale (equilibrium depth 20.5 cm) and some of the phenomena are thus scale dependent due to viscosity and surface tension. The amplification during shoaling, the wave overturning and breaking, as well as the initial formation of the large bubbles, are presumably only mildly dependent on scale. However, the disintegration of the bubbles is likely to differ from what would be observed in a tsunami, say, due to both scale and the use of fresh water versus brine. Moreover, the boundary layers will be turbulent on a larger scale and, probably, the turbulence will spread quickly through the small flow depth of the swash zone. Hence, results from this investigation may be conveyed to real applications in coastal engineering only with care.

Acknowledgement

This work was funded by the Research Council of Norway through the research project DOMT - Developments in Optical Measurement Technologies (project number 231491).

References

Barnes, M. P., O'Donoghue, T., Alsina, J., Baldock, T., 2009. Direct bed shear stress measurement in bore-driven swash. Coastal Engineering.

Cowen, E. A., A.M.ASCE, Sou, I. M., A.M.ASCE, Liu, P. L.-F., F.ASCE, Raubenheimer, B., 2003. Particle image velocimetry measurements within a laboratory-generated swash zone. J. Eng. Mech.

Dalziel, S. B., 2006. Digiflow user guide. `http://www.damtp.cam.ac.uk/lab/digiflow/digiflow.pdf`, [Online; accessed 20-Aug-2014].

Elfrink, B., Baldock, T., 2002. Hydrodynamics and sediment transport in the swash zone: a review and perspectives. Coastal Engineering 45 (3), 149–167.

Jensen, A., Pedersen, G. K., Wood, D. J., 2003. An experimental study of wave run-up at a steep beach. Journal of Fluid Mechanics 486, 161–188.

Kähler, C. J., Astarita, T., Vlachos, P. P., Sakakibara, J., Hain, R., Discetti, S., Foy, R., Cierpka, C., 2016. Main results of the 4th international piv challenge. Experiments in Fluids 57 (6), 1–71.

Lin, C., Kao, M.-J., Tzeng, G.-W., Wong, W.-Y., Yang, J., Raikar, R. V., Wu, T.-R., Liu, P. L.-F., 2015. Study on flow fields of boundary-layer separation and hydraulic jump during rundown motion of shoaling solitary wave. Journal of Earthquake and Tsunami 9 (05), 1540002.

Lin, C., Yeh, P.-H., Hsieh, S.-C., Shih, Y.-N., Lo, L.-F., Tsai, C.-P., 2014. Prebreaking internal velocity field induced by a solitary wave propagating over a 1: 10 slope. Ocean Engineering 80, 1–12.

Liu, P. L.-F., Park, Y. S., Cowen, E. A., 2007. Boundary layer flow and bed shear stress under a solitary wave. Journal of Fluid Mechanics 574, 449–463.

Pedersen, G., Lindstrøm, E., Bertelsen, A., Jensen, A., Laskovski, D., Sælevik, G., 2013. Runup and boundary layers on sloping beaches. Physics of Fluids (1994-present) 25 (1), 012102.

Peregrine, D. H., 1983. Breaking waves on beaches. Annual Review of Fluid Mechanics 15 (1), 149–178.

Petti, M., Longo, S., 2001. Turbulence experiments in the swash zone. Coastal Engineering.

Pujara, N., Liu, P. L.-F., Yeh, H. H., 2015. An experimental study of the interaction of two successive solitary waves in the swash: A strongly interacting case and a weakly interacting case. Coastal Engineering 105, 66–74.

Raffel, M., Willert, C. E., Wereley, S., Kompenhans, J., 2013. Particle image velocimetry: a practical guide. Springer.

Rivillas-Ospina, G., Pedrozo-Acuña, A., Silva, R., Torres-Freyermuth, A., Gutierrez, C., 2012. Estimation of the velocity field induced by plunging breakers in the surf and swash zones. Experiments in fluids 52 (1), 53–68.

Verschaeve, J. C., Pedersen, G. K., 2014. Linear stability of boundary layers under solitary waves. Journal of Fluid Mechanics 761, 62–104.

White, F. M., Corfield, I., 2006. Viscous fluid flow. Vol. 3. McGraw-Hill New York.